PAPER

Check for updates

Unravelling the highly efficient synthesis of individual carbon nanodots from casein micelles and the origin of their competitive constant-blue-red wavelength shift luminescence mechanism for versatile applications

R. Blessy Pricilla, [ID] David Skoda, [ID] Pavel Urbanek, [ID] Michal Urbanek, [ID] Pavol Suly, [ID] Eva Domincova Bergerova [ID] and Ivo Kuritka [ID] *

Synthesis of casein-derived carbon nanodots (CND) using a microwave-assisted approach, giving a high product yield (25%), is reported. Casein was used as a sustainable carbon source, and polyvinylpyrrolidone was used as a stabilizer for the nanodots. The size of the prepared amorphous CND corresponds to individual casein coils, which were only partially carbonized. They were obtained due to the disintegration of casein micelles and submicelles within the microwave-assisted solvothermal process. The resulting nanodots had bright photoluminescence, and their electronic structure and optical properties were investigated. A novel competitive model of their luminescence mechanism was introduced to explain a phenomenon beyond the standard models. The synthesized carbon nanodots were used as luminescent ink for anticounterfeit applications. A polymer matrix nanocomposite was prepared by dispersing the nanodots in a flexible and robust poly(styrene-ethylene-butylene-styrene) tri-block copolymer (SEBS) using the solution cast method. For the first time, the effect of CND on the luminescence and mechanical properties of the SEBS/CND self-supporting films was studied. The film was also studied as a phosphor for light-emitting diodes, with a unique experimental setup to avoid self-absorption, which results in low efficiency and eliminates the excess UV transmitted. Because of their high luminescence, photostability, and mechanical properties, these CND could be used as luminescent labels in the packaging and optoelectronics industries.

1. Introduction

Carbon nanodots (CND) are nanomaterials invading the current industrial era because of their exceptional features. As the name suggests, they belong to the carbon family, having a size of less than 10 nm. The nanodots typically consist of carbon, hydrogen, nitrogen, and oxygen.[1] They are expressed in terms of their carbogenic core and their functional groups present on the surface. Their core is disorganized, and a high amount of sp^3 carbons are present.[2] Furthermore, their properties can be modified by the level of oxidation present on their surface.[3] Since their discovery in 2004, they have been widely studied due to their remarkable properties like biocompatibility, good solubility, photostability, low toxicity, and less cost of preparation.[4–7] Due to their exceptional characteristics, different methods have been used for their synthesis like hydrothermal, solvothermal, microwave *etc.*[8–10] Depending on the synthesis method used hydrophilic, hydrophobic, or amphiphilic CND

are formed.[11,12] Their outstanding physicochemical properties attract their operations in different fields. Amongst all their exciting properties, their optical characteristics are widely studied because of their wonderful tuning quality. Their strong absorption and emission properties improve their effectiveness in hiding and storing essential information.[13]

Recently, cost-efficient and environment-friendly polymer/CND nanocomposites have been given much attention because of their marvelous attributes. These polymer/CND nanocomposites have enormous applications like luminescent solar concentrators, photocatalysis and metal ion detection and light-emitting diodes.[14–17] CND exhibit different luminescent colours in transparent polymers. Among the various polymers available, poly(styrene-ethylene-butylene-styrene) (SEBS) is an extremely strong and flexible tri-block copolymer. It consists of a hard segment called polystyrene and a soft segment called ethylene co-butylene, providing excellent thermo-mechanical properties. Additionally, it has excellent UV, heat and shatter resistance, toughness, and high transparency.[18] This suggests it to be an appreciable candidate for security and packaging applications.

Centre of Polymer Systems, Tomas Bata University in Zlin, Tr. T. Bati 5678, Zlin 76001, Czech Republic. E-mail: kuritka@utb.cz

In recent years, counterfeiting of authentic documents, brands, and products has been emerging as a serious problem. However, while advanced manufacturing has its benefits, the number of counterfeit goods is also rising due to the latest technological advances. Hence, various anticounterfeit materials and techniques are being explored to overcome this challenge. The anticounterfeit techniques make the original items difficult to duplicate and simple to validate, providing safety to official and valuable items.[19] Different types of technologies developed to reduce the fake transfer of data include holograms, latent fingerprint, security inks, and luminescent tags.[19–22] These technologies play an important role in the safety of the country and its people. While various kinds of techniques and materials have been used to regulate the counterfeit of goods, there has always been a search to obtain better materials that are cost-effective and easily produced. Currently, there is a growing trend to use luminescent photoresponsive materials as anticounterfeit materials.[23] Among the various luminescent materials available, specific attention has been given to CND, because of their excellent optical properties in the UV and visible light.[24,25] These nanodots, because of their high photostability, illumination rate and low toxicity, they have been effectively used to replace the conventional phosphors in LEDs.[26,27] Therefore, significant attempts are being made to understand and explore them, which is the necessity of the time.

In our paper, we have reported the synthesis of CND from the disintegration of casein micelles and submicelles using microwave-assisted approach. Compared to the traditional microwaves, the microwave reactor provides uniform heating, less by products and faster rate of synthesis. Casein is an easily available milk protein that has both hydrophobic and hydrophilic domains. It is a sustainable green source compound containing amino acids. It is a natural source of carbon. Polyvinylpyrrolidone (PVP) is used as a stabilizer to prevent the agglomeration of the nanodots. This high quantitative yield obtained through this method is suitable for large-scale production. Besides standard characterization, the electronic structure of CND and its photoluminescence mechanism are studied in detail. A new competitive model has been introduced to explain the luminescence mechanism of the nanodots. Flexible and robust SEBS/CND nanocomposite self-supporting film is obtained using the simple solution cast method. The luminescence and mechanical properties of the film were studied exclusively. According to the best of our knowledge, this is the first time to report the study on SEBS/CND nanocomposite film. We propose the application of the casein-based CND as anticounterfeit inks because of their good emission characteristics. The UV-sensitive luminescent nanocomposite films, because of their good transparency and photostability, can be efficiently used as anticounterfeit films for the packaging of products. Moreover, a peculiar experimental setup is developed to use SEBS/CND nanocomposite film as an efficient phosphor material for light-emitting diodes. Even though carbon dots have been utilized for these applications before, their product yield, synthesis with less time and appropriate temperature has always been challenging.[28,29] Sometimes the product yield is not reported or reported with no appreciable yield. In our work the microwave – reactor assisted method has proved to be an efficient method as it gives a high product yield (25%) in comparison with previous reports varying typically from 0.1% up to 19%.[30–32] Moreover, the product is obtained in less time and appropriate temperature with significant and exceptional characteristics.

2. Experimental section

2.1. Materials required

Polyvinylpyrrolidone (PVP), styrene–ethylene–butylene–styrene (SEBS) are obtained from Sigma Aldrich. Among many variable grades of milk protein concentrates (MPC) and milk casein concentrates (MCC),[33] a product "MPC 85 Micellar Casein" was acquired from a local retailer shop in the Czech Republic as a source of casein. The brand is a natural nutrition and unflavoured. MPC 85 is known for its content of *ca.* 71% casein, 11% of residual whey, 5% of residual lactose and minerals, and 1% of residual fat.[34] The powder was used before the best before date. The size of casein micelles was characterized experimentally in our laboratory which confirmed the suitability of the material for further studies. The distilled water was used for the preparation of various solutions. The polyethylene terephthalate (PET) foil (Novele™) used as substrates for printing was bought from Novacentrix, Texas, USA. A UV protection reflective window film "HooTown Mirror Window Privacy Film Self-Adhesive One-Way Silver Reflective Window Film UV Protection, Sun Protection and Heat Insulation Tinted Film, Silver" was brought commercially from amazon market. This film has 97% reflectance of UVA. The solvents, including ethylene glycol and isopropanol, are purchased from PENTA, Czech Republic. All the chemicals and reagents were used without any further purification.

2.2. Instrumental characterization

The CND particle size measurement was carried out using Transmission Electron Microscope (TEM). The TEM model, JEOL JEM 2100 microscope was operated at 300 kV (LaB$_6$ cathode, point resolution 2.3 Å equipped with OLYMPUS SYS TENGRA camera (2048 × 2048 pixels)). The size analysis of the particles was analysed by ImageJ software. The particle size distribution of the casein micelles dispersed in ethylene glycol before the synthesis was determined using Dynamic Light Scattering method (Zetasizer Nano ZS, model 3600, Malvern Instruments Ltd., Worcestershire, UK). The X-ray diffraction pattern was obtained from an X-ray powder diffractometer (Rigaku Miniflex 600) using Co Kα radiation ($\lambda = 1.7903$ Å), operated at a beam voltage of 40 kV and a beam current of 100 mA. A UV-Vis spectrophotometer, PerkinElmer Lambda 1050, was used to obtain the absorption studies. The emission studies were attained on photoluminescence (PL) spectrophotometer FLS920, Edinburgh Instruments (Xe lamp with a double monochromator used for excitation in continuous wave regime) at room temperature. Time resolved studies were performed using the same PL spectrophotometer with two different

excitation pulse diodes. One diode had an excitation wavelength 275 nm with a pulse width of 860 ps and another had an excitation wavelength of 332 nm with a pulse width of 840 ps. Both were operated at a frequency of 10 MHz. For both UV and PL experiments, 5 mg of the freeze-dried CND sample was dissolved in 5 ml of water. From this solution, 1 ml was taken and made up to 3 ml to perform the studies. Obtained spectra was corrected for both detector sensitivity and excitation source intensity. The Fourier Transform Infrared (FTIR) spectra analysis was carried out on Thermo Scientific Nicolet 6700 spectrometer utilizing the ATR method with the diamond crystal (4000–400 cm^{-1}, resolution 2 cm^{-1}, 64 scans). X-ray photoelectron spectroscopy (XPS) analysis was carried out using a Kratos Axis Supra spectrometer equipped with a monochromatic X-ray source with Al Kα excitation. The binding energy for C 1s at 284.8 eV was used as standard. The printing was achieved on the FUJIFILM DMP-2800 series Dimatix Materials Printer. The viscosity and density measurements of the ink were resolved on a Microviscometer Lovis 2000 ME (1.59 mm capillary) and Density meter DMA 5000 M (Anton Paar s.r.o., Prague, Czech Republic). The surface tension was measured by Tensiometer K100MK3 (Krüss GmbH, Hamburg, Germany) based on the Wilhelmy plate method. The compositional analysis was obtained on Flash 2000 CHNS/O+MAS200R, Thermo Scientific. The thermogravimetric analysis was executed on a Setaram LabSys Evo with TG/DSC sensor in an air atmosphere (heating ramp 5 °C min^{-1}, up to 1000 °C). The mechanical properties of the synthesized films were measured on a Testometric universal-testing machine of type M 350-5CT (Testometric Co. Ltd., Rochdale, UK). The contact angle studies were resolved on SEE System (Advex Instruments, Czech Republic). The total optical transmission of the samples was measured using a spectrometer Lovibond RT850i (Tintometer Limited) along with the ASTM D 1003.

2.3. Preparation of carbon dots derived from casein

CND were prepared using casein as a carbon source and PVP as a stabilizer. Various casein to PVP ratios were attempted to find a proper synthesis condition for CND within a preliminary heuristic phase of the research. While the ratio of components was free, the total volume of the Teflon-lined container in the monomodal reactor ERTEC Magnum II (600 W; 2.45 GHz) was given by its construction and used microwave wavelength. The initial amount of casein was always dispersed and mixed with ethylene glycol and PVP to obtain a sufficiently stable yellowish dispersion for the microwave processing. If the concentration of PVP was too low, the final product was in form of large agglomerates obviously unsuitable for production of CND. Increasing the concentration of PVP resulted into a well dispersed and clear final product brown solution at 1 : 2 casein to PVP w/w ratio. If the PVP concentration was further increased, irregular structures were obtained again.

Hence after the initial optimization, 0.1 g of casein was taken in a beaker, and 20 ml of ethylene glycol was added. This solution was kept for ultrasonication for 60 minutes to obtain a good dispersion. Ethylene glycol serves the dual purpose of

a solvent and a reducing agent. In another beaker, 0.2 g of PVP was taken and dissolved in 20 ml of ethylene glycol using ultrasonication for 10 minutes. Both the solutions were mixed and poured into a Teflon-lined container and kept in the microwave reactor. The reaction was carried out at 200 °C for 30 minutes with 100% (600 W) power. After cooling, the brown colour solution obtained was filtered using a 0.22 μm membrane filter. The filtered solution was dialyzed using a dialysis bag (3.5 kDa) for two days to remove the undesired low molecular side products or source compound residues. The solution was again centrifuged at 6000 rpm corresponding to a range from RCF$_{min}$ 1489 g to RCF$_{max}$ 5514 g all the undesired particles still remaining after dialysis. A centrifuge THERMO Multifuge X3R (Thermo Fisher Scientific, Germany) was used. Finally, the solution was freeze-dried for another two days to obtain the desired product. The product yield (PY) achieved through this method was calculated using the following formula.[35]

$$PY = \frac{m_{CND}}{m_{CA} + m_{PVP}} \times 100 \tag{1}$$

where m_{CND} refers to the mass of the CND obtained after lyophilization, m_{CA} refers to the mass of casein, and m_{PVP} refers to the mass of PVP. The product yield obtained using this calculation was found to be 25%.

2.4. Preparation of SEBS/CND nanocomposite film

For the preparation of SEBS/CND nanocomposite film, 20 wt% of SEBS solution and 0.25 wt% (C1), 0.5 wt% (C2), and 1 wt% (C3) CND solution were prepared in chloroform. Both the solutions were mixed in a 2 : 1 volume ratio and stirred for 60 minutes. After this period, the solution was cast on a Petri dish and covered to allow the film to dry slowly overnight. The next day the film could be easily peeled off from the Petri dish, and the desired characterizations were achieved.

2.5. Preparation of CND ink

The fluorescent CND ink was prepared by mixing the CND solution and ethylene glycol. Here, 1 wt% of the CND solution was prepared in water and mixed with ethylene glycol in a 2 : 1 volume ratio. Ethylene glycol is added to increase the viscosity of the ink. The prepared ink is mixed well using a sonicator for 10 minutes to obtain proper dispersion. The CND ink was loaded into the cartridge and kept in the cartridge holder. The temperature of the printer head nozzles was maintained at 30 °C. Similarly, the temperature of the PET foil, which was used as a substrate, was controlled at 40 °C.

2.6. Preparation of CND-LEDs

For the effective distribution of CND into the SEBS polymer solution, 2 ml of 2.5 wt% of CND dispersion in chloroform was added dropwise for 1 hour in 4 ml of 22 wt% SEBS solution of chloroform. After appropriate mixing, the mixture was allowed to be stirred for another hour. This mixture was drop cast on a Petri dish and dried overnight to obtain a uniformly distributed CND/SEBS polymer film. The film was mounted as a flat

layer on the LED device a wavelength of about 365 nm. To obtain maximum visible light a cut off filter of 395 nm and a UV protection reflective window film was placed on top of the CND/ SEBS polymer film.

2.7. Sample preparation for water contact angle studies

To determine the water contact angle (WCA), five measurements were carried out on the same PET substrate, using 5 μl of CND ink for each droplet. After placing a drop on the substrate the angle it formed with the film substrate was analysed using the system. Generally, if the contact angle is less than 90°, the substrate is hydrophilic; if the contact angle is more than 90°, the substrate is hydrophobic.

3.   Results and discussions

3.1.   Characterization of the carbon nanodots

The morphology of the synthesized CND is shown in Fig. 1(A). It is clear from the image that the nanodots are of different sizes. The TEM image shown helps in understanding the spherical nature of the particles. The average size of the particles as calculated by the ImageJ software was found to be 4.3 ± 1.1 nm.

Fig. 1(B) shows the XRD pattern of the CND. The broad peak at 18° of two theta corresponds to 0.57 nm interlayer spacing, thus indicating the amorphous nature of the CND,[36] rather than graphitization.[37,38] The thermal stability of the CND was analyzed using thermal gravimetric analysis in the helium atmosphere as shown in Fig. 1(C). The weight loss at around 100 °C can be attributed to the loss of small molecular weight compounds or adsorbed water. From around 260 °C to 450 °C, the decline observed is due to the decomposition of surface functional groups, the capping polymer, and likely some core components as well.[39,40] The residual mass at 800 °C is found to be 15.3%, which also testifies for low carbonization of the prepared CND and partial preservation of the structure of the precursor.

Table 1 shows the elemental analysis of casein and CND. The analysis was carried out to observe the change in the elemental composition between the precursor casein and the CND formed. The experiment was performed in three batches and their average was calculated. The elemental composition of carbon, hydrogen and nitrogen content in the CND was found

Table 1 Elemental analysis (wt%) of casein and carbon nanodots

Element	Casein (wt%)	Carbon nanodots (wt%)
C	46	56
H	6	8
N	12	10

to be 56, 8, and 10 wt%, respectively. The remaining wt% is assumed to be oxygen which is about 26 wt% in CND, while 36 wt% is in casein. The increase in the carbon wt% is evident due to the carbonization process.

An X-ray photoelectron spectroscopy (XPS) was employed to deeply investigate the bonding relations between elements in the synthesized CND sample as demonstrated in Fig. 2. The overview spectrum is not shown for the sake of brevity. The elemental ratio C : N : O was 76 : 10 : 13 in at% while the ratio among these elements from Table 1 is 65 : 10 : 23. The insignificant difference can be attributed to the experimental errors and differences between the two techniques due to different manifestations of carbon and moisture contamination in a vacuum apparatus and weighing in the ambient atmosphere for elemental analysis. In the C 1s XPS spectrum, four contributions were detected. These components with binding energies 284.9, 285.6, 286.7, and 287.9 eV are assigned to C–C/C=C, C–N, C–O, and C=O species, respectively. It should be noted, that no component is manifested at binding energy ~288.7 eV corresponding to the absence of carboxyl groups (O–C=O), excluding thus the presence of –COOH or ester groups. The O 1s XPS spectrum revealed the signals at binding energy 531.2 and 532.3 eV corresponding to O=C and O–C bonds, respectively. The N 1s XPS spectrum shows the main contribution at 400.0 eV, characteristic of the nitrogen atoms bound to carbon. Concerning the FTIR spectra and composition of the sample, the peak at 400.0 eV is most likely attributed to N–C=O amide bonds of the peptide backbone preserved from casein precursor after CND synthesis.[41,42] The same group in PVP may contribute to the intensity of the signal as well. The component at the higher binding energy side (401.6 eV) is attributed to NH or NH_2 species.[43] These findings also match the FTIR spectroscopy (Fig. 3(A)).
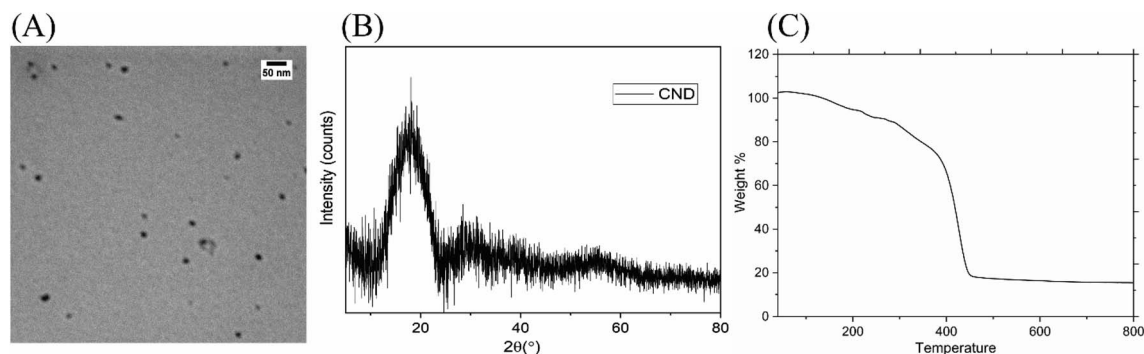

Fig. 1 (A) TEM image, (B) XRD pattern, and (C) TGA curve of the carbon nanodots in He atmosphere.
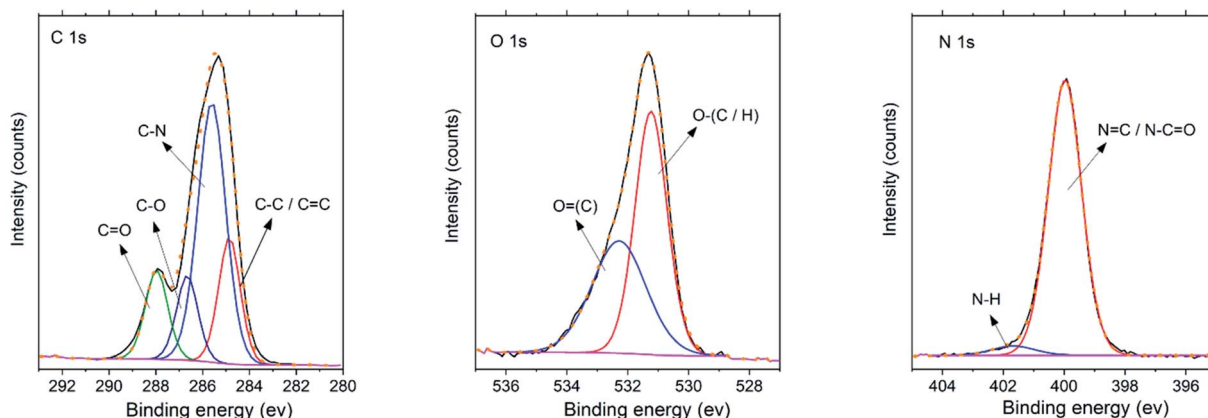
Fig. 2 The high-resolution XPS spectra of the CND sample.
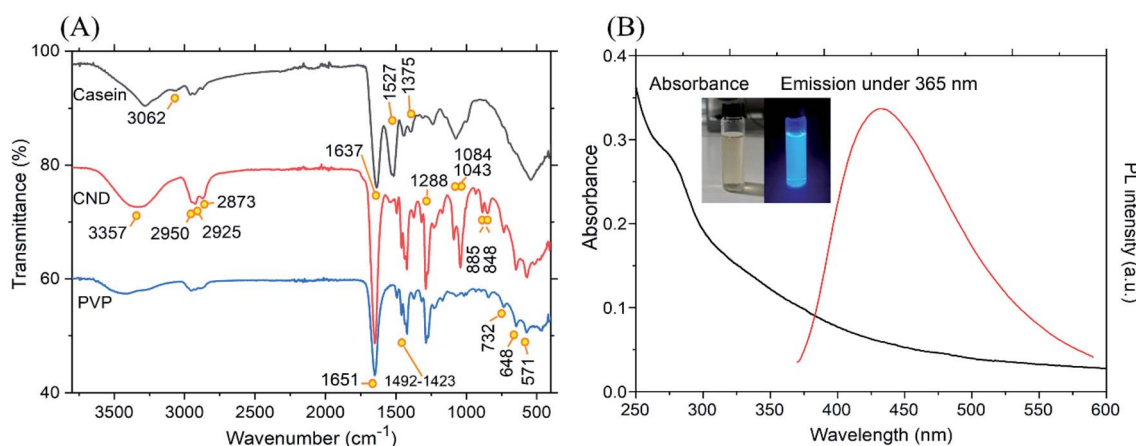

Fig. 3 (A) FTIR spectra of casein, CND and PVP and (B) absorption and an example of emission spectra of the CND at 365 nm.

The FTIR spectroscopy helps in the identification of the functional groups present in the CND. The FTIR spectrum of casein, CND and PVP is shown in Fig. 3(A). The FTIR spectra of CND is partially similar to that of PVP and casein. Moreover, it can be expected that the surface of the CND is covered with rich PVP chains.[44] The absence of certain bands from PVP and casein, as well as a shift in the position of the bands in the CND, indicate that a chemical reaction, rather than a physical interaction has occurred.

The presence of O–H and N–H vibrations in CND was confirmed by the broad vibrational band from 3600 cm^{-1} to 3100 cm^{-1} (CND-3357 cm^{-1}). Due to interactions with amide groups, the shoulder of this band expands extensively to lower wavenumbers in casein, whereas it is considerably inhibited in CND and absent in PVP. It may imply that the polymeric structure of the protein is degraded during the synthesis of CND. The band centered at 3062 cm^{-1} in casein corresponds to the valence vibration of CH bond in the aromatic system. Symmetric and asymmetric stretching of aliphatic CH at 2950 cm^{-1} and 2925 cm^{-1} (CH$_3$ ν_{as} and CH$_3$ ν_{sym}) and 2873 cm^{-1} with a shoulder at 2855 cm^{-1} (CH$_2$ ν_{as} and CH$_2$ ν_{sym}) are present in all the three spectra. The sharp vibrational band at 1637 cm^{-1} in casein and 1651 cm^{-1} in both PVP and CND is

due to C=O stretching vibrations (Amide I). Increased intensity of this band indicates the presence of large no. of amide (N–C=O) groups on the surface. Contrarily, the second typical absorption band classic for polyamides (including proteins) involving both C–N stretching and C–N–H in-plane bending in the stretch-bend mode (Amide II) is centred at 1527 cm^{-1} in casein and is largely suppressed in CND, though a distinguishable band of low intensity remains. This again testifies for a significant change of backbone structure during synthesis. A group of absorption bands at 1492, 1464, 1438, and 1423 cm^{-1} correspond to C–N and CH$_2$ scissor vibration and deformations of the cyclic side groups in PVP, which are observable in the spectrum of CND. A week absorption band at 1375 cm^{-1} is present in all three spectra yet slightly shifted to higher wavenumbers in casein. This band can be assigned to –CH$_3$ β_{sym} (umbrella) vibration, testifying to the presence of terminal CH$_3$ groups in the sample. The strong band at 1288 cm^{-1} in CND reveals the presence of C–N–H (Amide III) in the stretch-open mode of vibration. The other bands situated in the region of 1300 cm^{-1} and lower are related to C–H bending. The week bands above 1200 cm^{-1} (*i.e.* 1275, 1225 and 1214 cm^{-1}) indicate CH$_2$ wagging, C–N stretching and CH$_2$ twisting, which is confirmed by the week peak at 1169 cm^{-1}. The moderate and

strong peaks at 1084 cm^{-1} and 1043 cm^{-1}, reveal the presence C–O stretching in C–O–C and C–OH groups. The weak band at 885 cm^{-1} can be associated with CNC groups in amides or with oxygen-containing groups. The weak band located at 848 cm^{-1} is associated with the vibration modes for C–C bond in the pyrrolidone ring. Finally, the set of weak absorption bands at 732, 648, and 571 cm^{-1} are associated with CH$_2$ rocking vibrations, thereby confirming the manifestation of long aliphatic chains in both the CND and PVP spectra.[45,47] Altogether, the observed features testify for carbonization of the casein due to the partial destruction of peptide bonds in the original protein backbone, partial condensation of the aromatic groups and formation of ether and alcohol groups. On the other hand, no free carboxylic or isolated carbonyl groups (ketones, aldehydes, esters) were formed in the synthesis of CND as can be deduced from the absence of the carbonyl absorption band above 1700 cm^{-1}. Surface stabilization of the CND by PVP is also in line with features observed in FTIR absorption spectra.

The optical properties of the CND were studied using a set of characterizations. The UV-Vis absorption spectrum and emission spectra of the synthesized CND at 365 nm are manifested in Fig. 3(B). As can be observed, a small peak can be seen at 278 nm in the otherwise broad absorption spectra tailing over the visible range. The occurrence of the peak is accounted to the presence of π–π* transition of the aromatic C=C bond or n–π* transition of the C=O, =C–N, =C–O group as well.[26,48–50] This suggests the presence of isolated molecular-like states. However, these chromophores or fluorophores are rather a small molecular part or fragment than an edge or molecular state with an extended conjugated π-bond system. Indeed, there is no absorption peak between 300 nm and 400 nm in the spectrum (Fig. 3(B)) otherwise reported for CND with developed core, edge and surface states structure.[51] Generally, the spectrum resembles the typical spectral feature of a disordered semiconductor which may be likely due to both structural irregularity and the size distribution of particles.[52] The UV-Vis absorption spectrum is deeper analyzed in Fig. 4(A) and (B). Understanding the optical properties of CND remains difficult, as they usually lack a well-defined electronic band structure and have fluctuating properties that vary between sources (*e.g.* source compound, synthesis method, degree of carbonization, crystallinity or amorphousness, polydispersity). Despite such complexity, Tauc band gap can be considered as a phenomenological parameter for comparison.[53,54] Hence, the Tauc plot was constructed.[55] In Fig. 4(A), a best linear fit for allowed indirect transition between the valence band (VB) and the conduction band (CB), yielding $E_{g1} = 1.8$ eV was attained. The linear part of the spectrum in the Tauc plot (T$_1$ region) spans approximately from 3 eV to 4 eV (420–310 nm). Above 4 eV, a peak may be observed due to the transitions associated with isolated chromophores. The absorption edge of the CND is not abrupt, and the absorption tail extends deep into the forbidden gap. Thus, at lower energies (*i.e.* <3 eV) a manifestation of structural disorder is observed.[56,57] Two separate strictly linear parts of this tailing region were identified at lower wavelengths (2.95–2.65 eV and 420–466 nm) ascribed as Urbach tail (U

region) and at higher wavelengths (1.55–2.40 eV and 800–516 nm) assigned as weak absorption tail (WAT).[54,56,58–60]

The Urbach tail is related to the disorder, defects, and thermal vibrations in the lattice of a material. They are associated with the transitions from localized electronic centers to extended states or *vice versa*, but the latter is considered less probable. This region is analyzed when plotted in the ln scale in Fig. 4(B). The following equation can be used to determine Urbach energy, which expresses how absorbance (α) scales with photon energy ($h\nu$).[58]

$$\alpha(h\nu) \sim e^{h\nu/E_U} \tag{2}$$

Thus, the Urbach energy (E_U) may be calculated from the reciprocal slope of the linear portion in Fig. 4(B). The high value of the Urbach energy 0.93 eV obtained for the CND indicates a large structural disorder and broad distribution of localized states. Although these states are usually associated with surface defects,[51,57] we expect many defects in the whole structure of our CND as it is amorphous without any sign of a crystalline core structure.

The lowest part of the absorption edge is the WAT region and is related to the purity and perfection of the material. It involves transitions between localized defect states. It is calculated using the following equation.[58]

$$\alpha(h\nu) \sim e^{h\nu/E_{WAT}} \tag{3}$$

The reciprocal slope obtained from the linear portion of the curve in Fig. 4(B) yields weak absorption tail energy (E_{WAT}). The E_{WAT} is always larger than E_U. The high value 1.18 eV of E_{WAT} suggests the presence of significant populations of localized tail
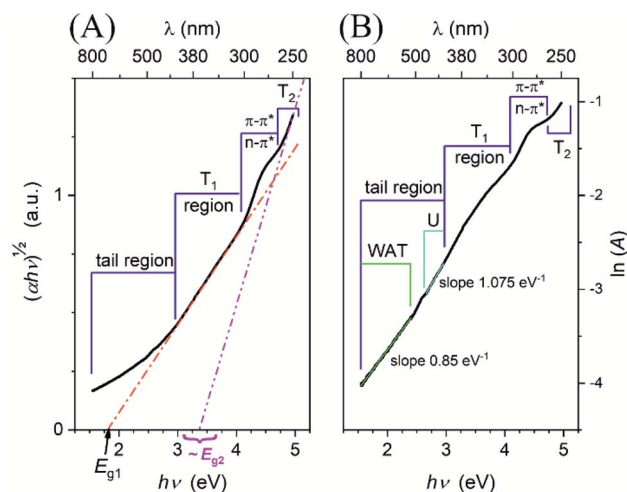

Fig. 4 (A) Tauc plot for indirect allowed transition and (B) absorption spectrum in natural logarithm scale replotted against absorbed light energy for band gap tail analysis, where U represents Urbach tail region, WAT stands for weak absorption transition region, T$_1$ indicates the region corresponding to the linear part of the Tauc plot (band gap E_{g1}) and T$_2$ is used for the second band gap region (E_{g2}). Corresponding electronic transitions are assigned to the prominent part of the spectrum.

     © 2022 The Author(s). Published by the Royal Society of Chemistry

states and deep band gap states in the electronic structure of the CND. Such rich and wide distribution of defects was inbuilt, most likely due to partial carbonization of casein macromolecules.

When the solution of CND was illuminated with a UV lamp of 365 nm, blue fluorescence was obtained as illustrated in Fig. 3(B). The absolute quantum yield obtained using the integrating sphere was found to be 4%. The observed excitation-dependent property of the CND is one of their distinguishing emission characteristics.[61] A PL emission spectra was recorded for excitation wavelengths 250 nm to 310 nm (Fig. 5(A)) and for excitation wavelengths 320 nm to 420 nm (Fig. 5(B)). A common scale bar of the 3000 arbitrary unit size is shown in both figures to enable intensity comparison. Several trends can be observed in the PL spectra in Fig. 5(B). Firstly, a red-shift in the PL emission maxima ($\lambda_{em,max}$) is observed with an increase in

excitation wavelength (λ_{ex}) above 320 nm, which implies a relatively simple band structure of CND.[54,62] Secondly, the intensity of PL emission increases up to a maximum of 442 nm when excited at 370 nm and then decreases with a further increase of λ_{ex}. The initial increase in PL intensity may be due to the diminishing self-absorption effect or intersystem conversion. According to the literature, the bathochromic shift observed with decreasing intensity might be due to low optical absorption in the visible range or due to surface defects because of the high level of surface oxidation.[51,63] The latter possibility seems to be inappropriate in our case, according to the FTIR and XPS analysis. These PL findings correlate with the PL mechanisms like quantum confinement theory and the surface state model of CND.[54] However, more than one radiative relaxation channel is observed in Fig. 5(A) ($\lambda_{ex} \leq 320$) as indicated by the dot and dash lines connecting corresponding PL emission maxima
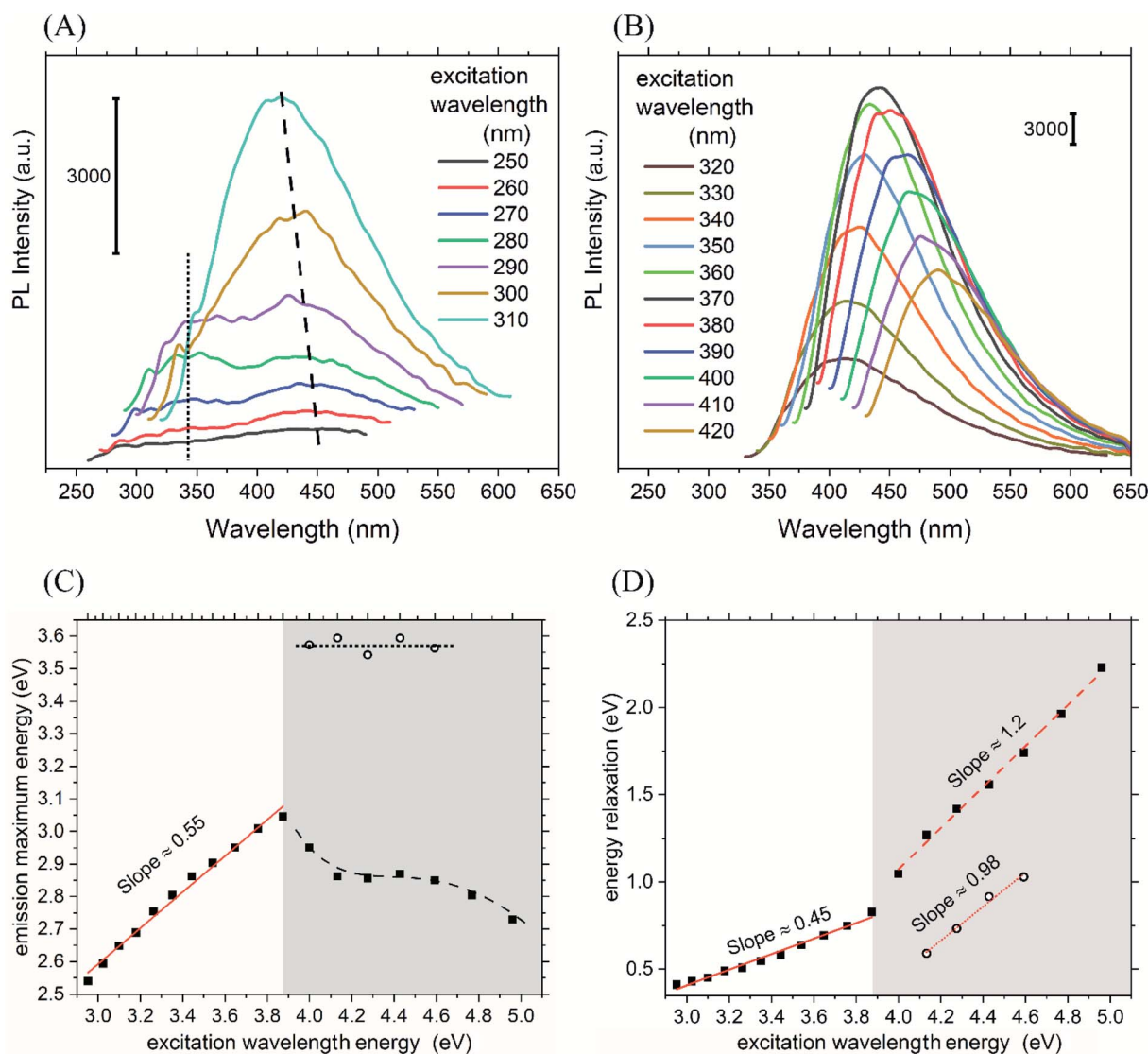

Fig. 5 The graphs (A) and (B) show PL emission spectra of CND excited at variable wavelengths. The graph (C) shows the dependence of the PL emission maximum energy and wavelength on the used excitation energy. The graph (D) indicates relaxation energy as the difference between PL emission maximum energy and excitation energy plotted *versus* the excitation energy. White and shaded area delimits the two PL modes in graphs (C) and (D).

($\lambda_{em,max}$). It is noteworthy that the maximum at lower wavelengths (at ~347 nm) does not change its position with the change of λ_{ex} while the maximum at higher wavelengths blue-shifts. This mechanism is analyzed in terms of energy bands and indirect transitions below.

The PL emission with fixed $\lambda_{em,max}$ in the UV range was already observed for carbon dots in carbon nitride nanoflakes and can be attributed to isolated fluorophores in our case as well.[57] Although molecular state mechanism is expected for bottom-up synthesized CND, it mostly works well when the PL emission is not excitation-dependent.[54,64] There are three common amino acids in casein, namely phenylalanine (Phe), tyrosine (Tyr), and tryptophan (Trp), exhibiting intrinsic fluorescence. It is expected that their residues are present in the synthesized CND. The observed transition at ~347 nm fits most likely to the luminescence of Trp. Phe and Tyr transit at shorter wavelengths and may be involved in the UV emissions in 260–310 nm. Their luminescence may be lowered due to the energy transfer between them due to their spectral match.

A more elaborate analysis of the observed phenomenon in terms of energy can be seen in Fig. 5(C) and (D). The full squares in Fig. 5(C) represent the energy ($h\nu_{em,max}$) corresponding to $\lambda_{em,max}$ observed at the higher λ_{ex}, and the empty circles represent $h\nu_{em,max}$ corresponding to the $\lambda_{em,max}$ observed at the lower λ_{ex}. The difference between $h\nu_{em,max}$ and $h\nu_{ex}$ in Fig. 5(D) is interpreted as the vibrational relaxation energy or even intersystem crossing relaxation energy. The two regions below and above 320 nm in Fig. 5(C) and (D) are distinguished by light grey colour. As shown in Fig. 5(C), for λ_{ex} above 320 nm, the $h\nu_{em,max}$ obeys a single linear dependency on the $h\nu_{ex}$ with the slope value ~0.55. This is comparable to the decreasing relaxation energy in Fig. 5(D) with a slope of 0.45, resulting in zero relaxation energy for $h\nu_{ex} \approx 2.0$. This value correlates well with the first band gap energy (E_{g1}) 1.8 eV. Hence, it is expected that the luminescence will vanish at about 620 nm.

Interestingly, two features were revealed at the higher excitation energy region below 320 nm. Firstly, the open circle symbols with constant energy (horizontal) dot line represent the radiative transition channel that is independent of λ_{ex}. It can be associated with the isolated fluorophores most likely Trp residues as discussed above. A similarly simple pattern is seen (for open circles) in Fig. 5(D), where the energy difference decreases with unity slope, and zero relaxation energy is observed at 3.6 eV. This corresponds perfectly with the fixed emission wavelength ~347 nm. The point at $h\nu_{ex} = 4.0$ eV (310 nm) shows the almost vanishing emission intensity, which is in agreement with the absorption edge of Trp. Secondly, the emission maxima (full squares) blue-shifts with increasing excitation wavelength in Fig. 5(C), which is manifested as diminishing progression of the relaxation energy with the slope 1.23 yielding zero relaxation energy for 3.15 eV in Fig. 5(D). This could indicate a splitting of the CB into two (CB_1 and CB_2), which is also consistent with the PL quantum confinement theory of CND (size of the CND ~ 4 nm). This is the size range for eventual moderate quantum confinement effects in CND.[46,65]

To verify the presence of three possible radiative deexcitation mechanisms and investigate their nature, time resolved PL experiment was performed. A double exponential decay was used for fitting the data and an average lifetime $\bar{\tau}$ was calculated according to the eqn (4)

$$\bar{\tau} = \frac{\alpha_1 \tau_1^2 + \alpha_2 \tau_2^2}{\alpha_1 \tau_1 + \alpha_2 \tau_2} \qquad (4)$$

where α_i and τ_i are the parameters of the model.[66] The dimensionless α_i represent pre-exponential factors and τ_i stands for lifetimes of the two fluorescence decay components. The values of the pre-exponential factor α_i depend on the emission center concentrations, their absorption coefficient, quantum yields, and intensities of each radiative pathway at the used excitation wavelength. The results are summarized in Table 2.

A revision of the Tauc plot enables hypothetical linear extrapolation of the absorbance curve at highest energies showing the second gap (E_{g2}) between 3 and 3.7 eV with the value ~3.3 eV as the best guess (Fig. 4(A)). It is expected that the LUMO of the isolated fluorophore (possibly Trp) is partially located in the second conduction band (molecular state). For corresponding transitions emitting constantly at ~347 nm, the lifetime analysis confirmed fluorescence lifetimes. These were similar to those of tryptophan residues in proteins existing in two conformations (with corresponding $\tau_1 = 0.94$ ns and $\tau_2 = 3.35$ ns) with the average lifetime about 2.2 ns (Fig. 6(A)).[67] It is anticipated that the electrons excited to the higher extended states have two different ways of radiative relaxation. Either the excited electron relaxes until trapped at the localized fluorophore and the energy is released at the fixed wavelength ($\lambda_{em,max}$ ~ 347 nm), or the excited electron may relax within the CB_2, and then radiative recombination at a higher wavelength may occur. The closer the $h\nu_{ex}$ energy is to the $h\nu_{em,max}$ (~3.6 eV), the less energy relaxation can be observed. This suggests some extinguishing of extended vibrational states in proximity to the isolated fluorophore energy level which works as a trap. Therefore, the lifetime was measured for emission at 430 nm

Table 2 Lifetimes of PL emissions of carbon nanodots excited by two different sources

Excitation wavelength (nm)	Emission wavelength (nm)	Lifetime analysis results				
		α_1 (—)	τ_1 (ns)	α_2 (—)	τ_2 (ns)	$\bar{\tau}$ (ns)
275	347	0.055	0.94	0.017	3.35	2.20
275	430	0.044	1.25	0.017	6.62	4.85
332	430	0.036	1.85	0.012	8.30	5.71
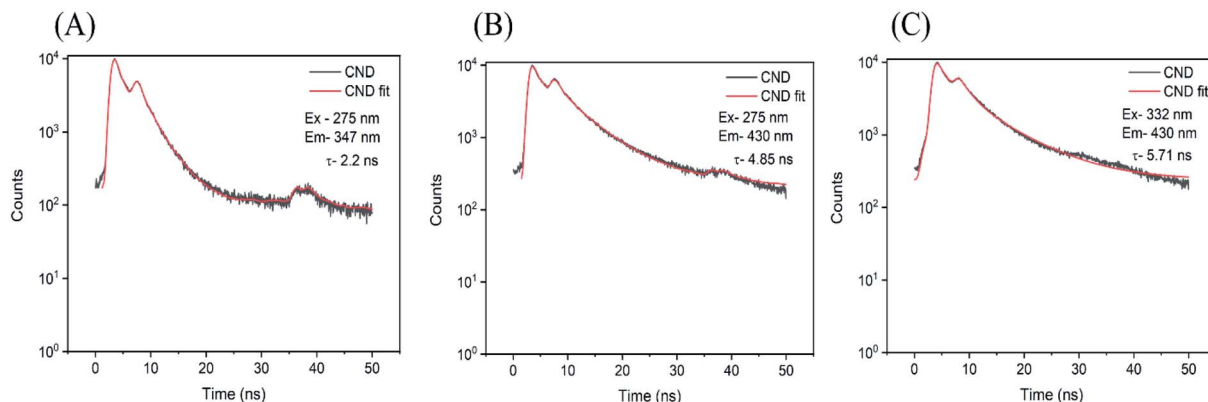
Fig. 6 Lifetime analysis of CND fluorescence at (A) λ_{ex} 275 nm and λ_{em} 347 nm (B) λ_{ex} 275 nm and λ_{em} 430 nm (C) λ_{ex} 332 nm and λ_{em} 430 nm. Double exponential decay model was used and average lifetime is indicated in the graphs.

excited by the 275 nm wavelength light, exactly the same as for the Trp fluorophore. A long average lifetime of 4.85 ns, typical for carbon dots was obtained (Fig. 6(B)).[68,69] The short living component $\tau_1 = 1.25$ ns is quite close to the one of Trp while the long living component $\tau_1 = 6.6$ ns suggest a slow energy relaxation in an extended energy level system. It can be hypothesized that electrons excited to higher energies may live longer and relax to lower energies since there is less probability for them to be trapped at the fluorophore. In contrast, for excited electrons closer to the fluorophore lowest vibrational level, less time is available for the energy relaxation of the electron because of its high probability of being trapped. The third lifetime experiment was performed to verify the nature of typical CND luminescence dependent on excitation wavelength as observed for excitations below 3.9 eV in our case. The average lifetime of emission at 430 nm pumped by 332 nm pulses showed slow relaxations typical for extended electronic states for both components $\tau_1 = 1.85$ ns and $\tau_2 = 8.30$ ns with an average lifetime of about 5.7 ns (Fig. 6(C)).[39,68]

The different types of electronic transitions observed in the CND are summarized in Fig. 7 for improved understanding. The energy level diagram in Fig. 7(A) shows the two identified bands and their possible absorption transitions. It is noteworthy that the Urbach and WAT transitions cannot contribute to the observed UV and visible luminescence features due to their small energy which discriminates the standard surface state PL model from consideration. Although the simple band diagram corresponds to the absorption spectrum in Fig. 3(B) and its analysis in Fig. 4(A) and (B), it cannot fully explain the blue shift of PL emission concurrent and the fixed wavelength emission in the UV region. Hence, a new model is given to reflect the indirect allowed transition between the extended ground states in VB and extended states in CB_1 or CB_2. Such transitions are likely to occur in a defect-rich semiconducting material. In the band diagram of Fig. 7(B) the vertical arrow indicates the direct transition to the molecular state (MS), while the indirect transitions are depicted by inclined arrows. The vibrational relaxations are indicated by curved arrows in Fig. 7(B) and (C). The electrons (red asterisks) excited by the energies higher than 3.9 eV have such energy that they may follow either of the two possible relaxation pathways.

The first channel (1) towards the left in Fig. 7(C) involves the trapping of the electron at the fluorophore followed by a fast relaxation to its lowest excited state and fast emission. The
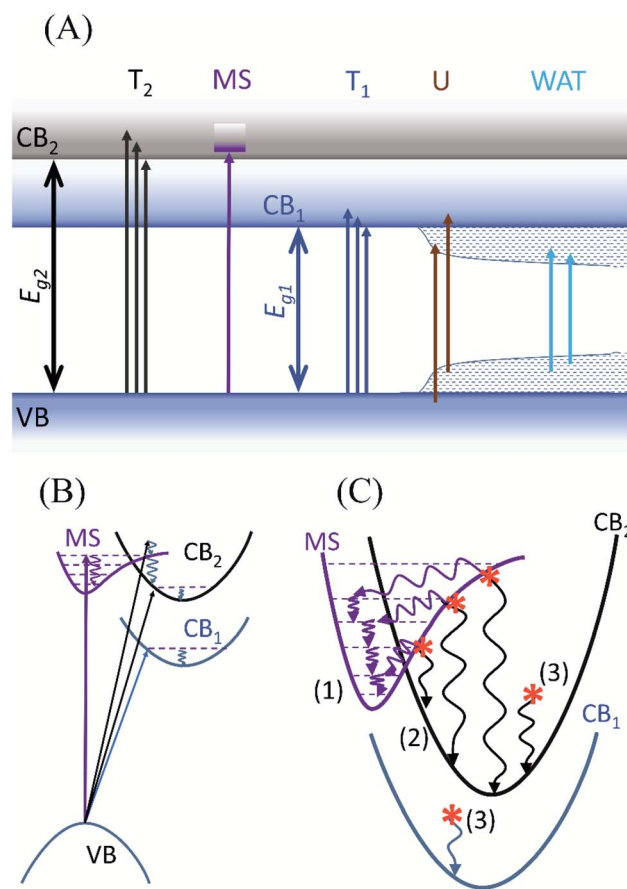

Fig. 7 (A) Schematic representation of various electronic transitions taking place between the valence and the conduction band. (B) The two different emission pathways responsible for the blue shift in the PL spectrum. (C) Magnified image of the electronic transitions happening in the conduction band and the molecular states (T_1 and T_2-the two Tauc regions, MS-molecular state, U-Urbach transitions, WAT-weak absorption transitions, E_{g1} and E_{g2}-two band gaps, CB_1 and CB_2-two conduction bands, the numerals in brackets indicate radiative channels as explained in the text).

second channel (2) towards the right goes through relaxation in the CB_2. As the indirect radiative recombination involves phonon or defect interaction, it takes a longer time than a direct deexcitation from the fluorophore. Therefore, the excited electron has a chance to pass through the indirect band channel only before it is caught by the trap, which results in its limited relaxation manifested as the observed blue shift. To complete the picture for excitations below 3.9 eV, the third radiative channel (3) is the standard one between CB_1 and VB or CB_2 and VB with vibrational relaxations. This results in the red shift of slower PL emission maximum with the diminishing progression of the difference between λ_{ex} and $\lambda_{em,max}$. For the sake of simplicity, the arrows indicating radiative and other deexcitations are not shown. As none of the three standard models known for carbon nanodots can explain sufficiently the observed luminescence phenomena,[46,49,58,59] we introduced the above-described model under the name "competitive model". The name is suggested due to the competition between the first and second radiative deexcitation channels present in the electronic structure of the prepared CND.

3.2. Mechanism for the synthesis of CND

Based on the spectroscopic and microscopic characterization, a synthesis mechanism of CND has been described. For most common proteins, the standard mechanism of carbon dots synthesis from macromolecular sources follows a process of denaturation, aromatization and nucleation.[8,70] However, in our case, another mechanism has been introduced to explain the nature of the reaction. Ethylene glycol is a solvent highly absorbing microwave radiation, enabling rapid heating of the reaction mixture. Casein obtained from bovine milk is polydisperse, having spherical colloidal particles of 50–600 nm. These are called "casein micelles" with an average diameter of ~150 nm.[71] In our case, casein was dispersed in ethylene glycol, and its micellar nature was restored before microwave processing. The average diameter of particles obtained after the ultrasonication of the dispersion was 497 nm (with DLS PDI 0.51) according to the DLS measurements. This indicates that the ultrasonication did not destroy the structural integrity of the casein micelles before microwave processing. The resulting CND are of two orders of magnitude smaller, about 4 nm. The diameter of the submicelles consisting of 20 to 25 casein molecules is 12 to 15 nm.[72] The number of the casein coils (25) in the submicelle (15 nm) indicates a diameter of about 5 nm for a single casein coil. It is reasonable to expect that the casein micelles were disintegrated into submicelles which were further fragmented into individual casein coils by the fast microwave heating. Further, the denatured casein coils are partially carbonized into CND, retaining still some moieties and structural features of the casein source. The solvent molecules neither take part in transesterification reactions nor allow oxidation. The presence of PVP forms most likely a capping layer around the CND and prevents them from forming agglomerations.

3.3. SEBS/CND nanocomposite film

To verify the use of the nanocomposite films for anticounterfeit application, the films were tested under visible and UV light as shown in Fig. 8(A). When the film was irradiated
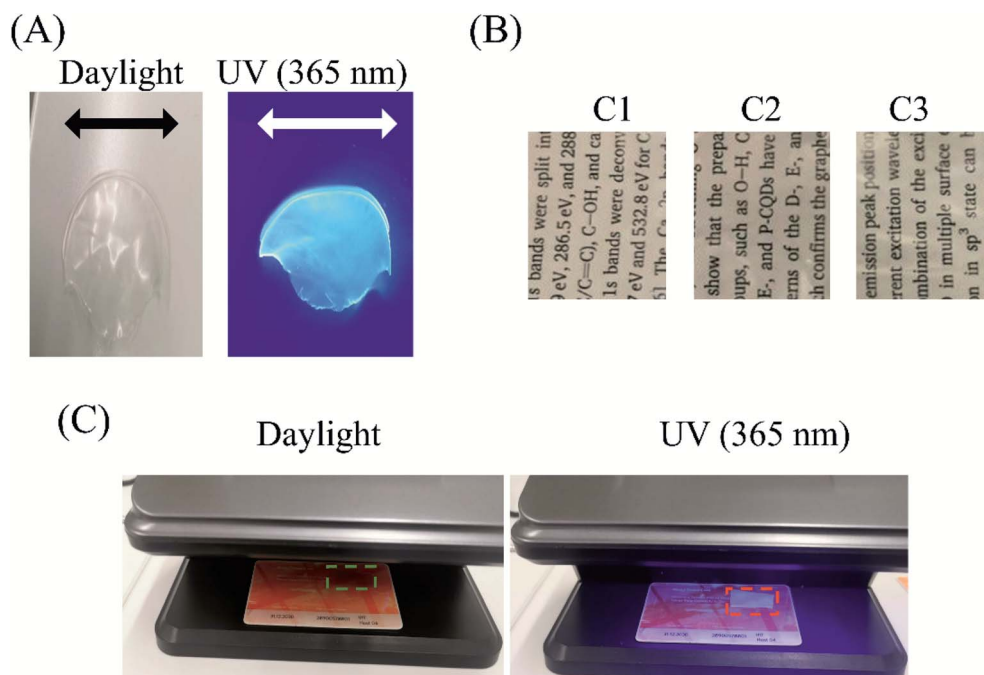

Fig. 8 (A) SEBS/CND nanocomposite film under visible and UV light (365 nm). The film was cast in a Petri dish of the diameter 8 cm. The photographs were taken at different places and from different viewing angles. Therefore, the diameter is indicated by the black and white double-sided arrows added to the images. (B) Visible light transmittance through the films. (C) SEBS/CND polymer films on a guest card of TBU under daylight only and with UV lamp (365 nm) switched on.

with a UV lamp (365 nm), the film emitted a blue fluorescence. However, under visible light conditions, the film appears to be colourless. These results show that the prepared SEBS/CND nanocomposite film is UV sensitive and can be used for anti-counterfeit applications.

The light transmittance through these nanocomposite films was studied along ASTM D 1003. It was observed that the composite film (0.5% CND) had optical transparency of 45%. To visually observe the transparency, we kept the synthesized films with different compositions of CND over some text. As can be seen in Fig. 8(B), the letters in the text are visible even up to 1% CND concentration. Fig. 8(C) shows SEBS/CND polymer films on a guest card of Tomas Bata University. The figure beautifully depicts the transparency of the film in the daylight; however, when the films were exposed to a UV banknote detector of wavelength 365 nm, the bright luminescence of the films is observed. Hence, these films can be effectively used in the packaging industries and for anti-counterfeit applications.

3.3.1. Fluorescent stability under UV irradiation. To estimate the stability of the synthesized SEBS/CND nanocomposite film under UV illumination, the film was exposed to UV irradiation (450 W) for a particular period, and their corresponding fluorescent intensity was measured under an ambient atmosphere. A fixed slit width of 1 μm was maintained with a UV irradiance of 0.20 mW cm^{-2}. The change in fluorescent intensity with increasing time is shown in Fig. 9. As demonstrated, a decrease of up to 30% is observed in the fluorescent intensity up to four hours, after which there are negligible changes in the fluorescent intensity. These experiments show a good photostability of the SEBS/CND nanocomposite film even with prolonged exposure to UV irradiation.

3.3.2. Mechanical properties. The mechanical property of the SEBS/CND nanocomposite was studied and their stress–strain curve analysis is depicted in Fig. 10. It is observed that the nanocomposite film can take more stress as compared to SEBS. This indicates the good interaction between the filler (CND) and the matrix.
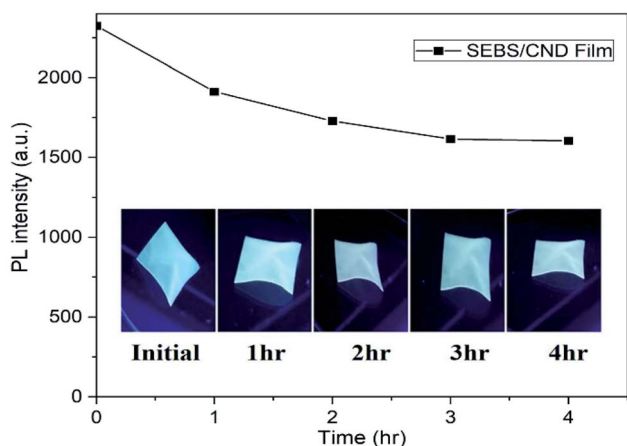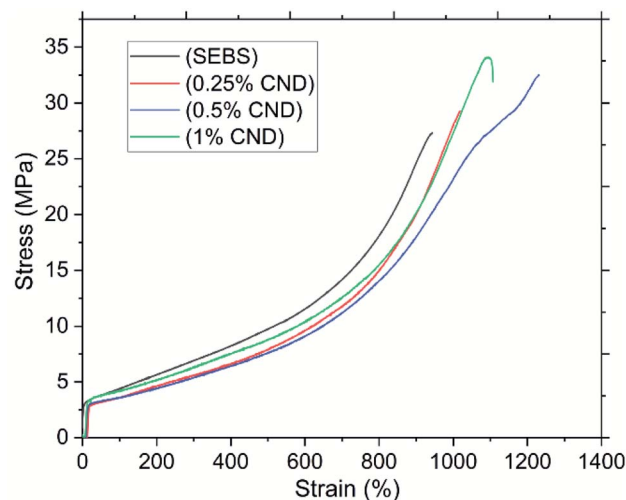

Fig. 10 Stress–strain curves of SEBS and SEBS/CND nanocomposite film – one curve selected as an example for each sample.

The elastomer characteristics were observed in the strain, with the increase in the concentration of the CND filler, the strain at break increases from *ca.* 900% to *ca.* 1200%. This shows that the addition of filler increases the resistance of the nanocomposite film. However as can be seen, with the increase in the concentration of the filler to 1%, a decrease in the strain is observed. This can be attributed to the fact that with the increase in concentration, the particles tend to agglomerate leading to the break of the nanocomposite film.[73] The Young's modulus of the pristine SEBS and the nanocomposite film was found to be (97 ± 8) MPa and (77 ± 9) MPa (C3), respectively. This decrease in the Young's modulus can be accounted to the presence of cracks and pores in the nanocomposite film or to poor adhesion of the filler and matrix. It may also be due to the very different nature of SEBS and PVP, which are normally immiscible and only copolymer grafting results in compatibilisation.[74]

3.4. Carbon nanodots as anticounterfeit ink

To demonstrate the application of CND as anticounterfeit ink, we created some patterns on a PET substrate. Inkjet printing was used to obtain the desired patterns of the CND ink. The dynamic viscosity, surface tension, and density of the CND ink are measured to be 2.263 mPa s, 41 N m^{-1}, and 1.04 g cm^{-3}.

Fig. 11(A) depicts an image of the printed patterns from CND ink with and without the presence of UV (254 nm). The motif is practically invisible in daylight. However, when the patterns were excited at 254 nm using a UV lamp, the patterns emitted an intensive blue fluorescence. Excitation of the patterns by 365 nm wavelength resulted in a less prominent fluorescence on the substrate. These results indicate the effectiveness of the CND to be used as anticounterfeit ink for printing. As seen in Fig. 11(B), the compatibility of the CND ink with the PET substrate was analyzed using water contact angle studies. Five measurements were carried out on the substrate at different places. Their average was calculated to be 18.24°. This indicates the hydrophilic nature of the ink towards the substrate.
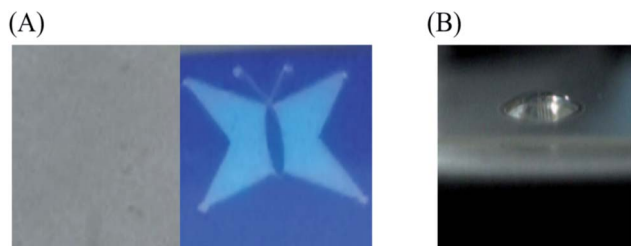

Fig. 9 UV stability test of SEBS/CND nanocomposite film using fluorescence spectra.

Fig. 11 (A) Printed pattern from the CND ink on PET substrate with (right) and without (left) UV (254 nm). (B) Water contact angle on PET substrate.

Fig. 12(A) shows the thermal stability of the ink, which was analyzed by treating the printed patterns at three different temperatures 60 °C, 90 °C, 120 °C. The patterns were kept at each temperature for 60 minutes. As observed in Fig. 12(B), the PL intensity of the untreated PET substrate with the ink has less luminescence as compared to the treated PET substrates with the ink. As apparent from the spectra, the luminescence of the

ink substrates treated at different temperatures remains almost the same with their maximum red shifted due to prevalent agglomerations with increase in temperature. This indicates a good thermal and photostability of the CND ink.

3.5. Application of CND as phosphors in LEDs

To demonstrate the ability of CND as phosphors, a CND-based phosphor LED was created by layering SEBS/CND nanocomposite film on top of a UV chip with an excitation wavelength of about 365 nm. The luminescence spectra with the operating device and the chromaticity diagram with the final colour of the device is displayed in Fig. 13(A) and (B).

Phosphors based on materials with maximum emission wavelength dependent on the excitation wavelength may suffer from problems like self absorption and long wavelength emission. As a result of these factors, the device's efficiency is reduced. These problems were eliminated to a great extent by a proper selection of the film thickness and concentration of CND. Moreover, a commercial reflective UV protection window
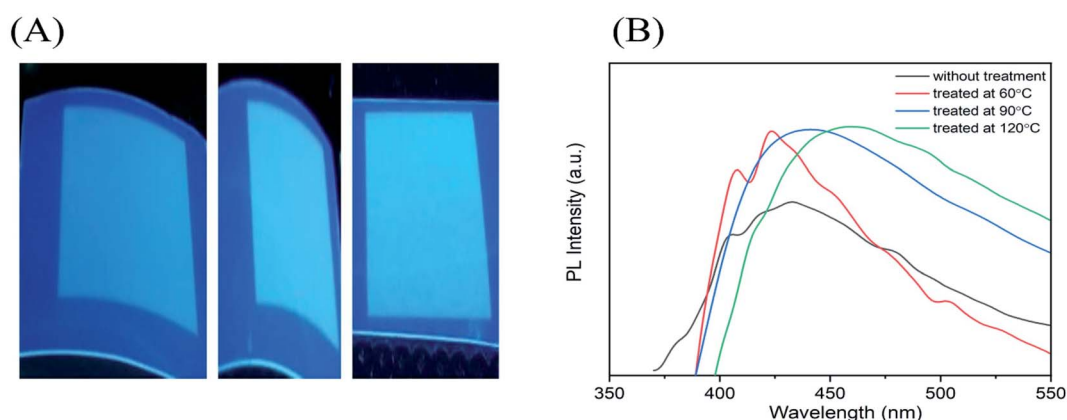

Fig. 12 (A) Thermal treatment of the printed CND ink at 60°, 90°, and 120 °C. (B) PL spectra of the printed CND ink without and with heat treatment at 60 °C, 90 °C and 120 °C. PL spectrum of the substrate was subtracted.
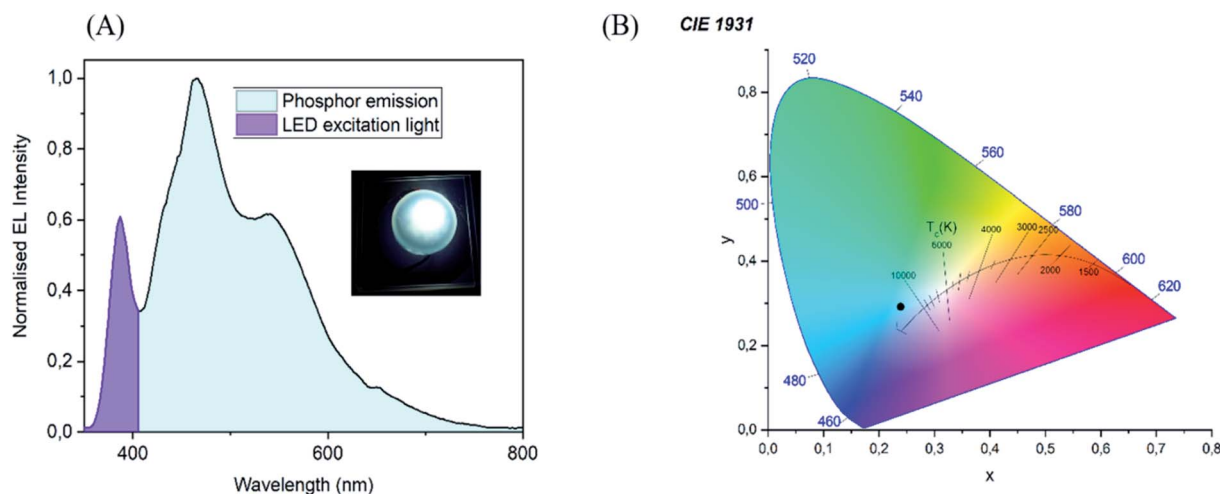

Fig. 13 (A) Luminescence spectra with operating device at 365 nm (B) chromaticity diagram.

film was used to enhance the efficiency of CND luminescence. As this was just a preliminary optimization, a cutoff filter at 395 nm was used to suppress the excessive excitation UV light coming through the phosphor film. Further development is necessary to fully optimize the device, however, this is beyond the scope of this article.

4. Conclusions

In summary, the synthesis of casein-based CND has been successfully achieved using a microwave-assisted approach. The advantage of this method is its high product yield of about 25% with respect to the initial weight of casein precursor and PVP stabilizer. A synthesis mechanism has been deduced. Casein micelles were quickly disintegrated into submicelles, which were then separated into individual casein coils of the size that corresponded to the CND. The casein coils were only partially carbonized, and the resulting amorphous CND still included certain structural motifs and chemical moieties from the original source. Regarding the electronic properties, CND showed blue fluorescence when irradiated with a UV lamp (365 nm), and the emission properties manifested excitation-dependent PL characteristics. The unique blue shift followed by red shift in the PL spectra and the portion of UV luminescence independent on the excitation wavelength stands out to be an exciting property of the casein derived CND, which has a scope to be explored more. The mechanism underlying these luminous characteristics can be explained by a new competitive model which is beyond the standard models in CND. The observation of Urbach and WAT region tailing deep into the band gap in the absorption spectrum gave a new perspective to understand the defects and disorders in the electronic structure of CND. The solution cast method was utilized to obtain a flexible SEBS/CND nanocomposite film with good photostability, optical transmittance, and mechanical properties. The synthesized CND has found its application in anticounterfeit market for polymer ink with appreciable thermal stability. The free-standing luminescent nanocomposite film can be effectively employed as anticounterfeit films for packaging and security applications. The potential of CND as phosphor material for LEDs as has been suggested in the work using a unique experimental setup which eliminates excess of UV transmission and avoids self absorption resulting in lower efficiency. Moreover, the transparency attained by this polymeric nanocomposite makes it to be a promising candidate for possible applications in information technology, defense system, transportation, and environmental protection. The promising results obtained and the characteristics like nontoxicity, easy preparation, cost effectiveness of CND makes it a good phosphor material to be used for multipurpose applications.

Author contributions

R. Blessy Pricilla: conceptualization, methodology, investigation, formal analysis, visualization, writing – original draft. David Skoda: conceptualization, methodology, investigation, supervision. Pavel Urbanek: investigation. Michal Urbanek: investigation. Pavol Suly: investigation. Eva Domincova Bergerova: investigation. Ivo Kuritka: conceptualization, methodology, formal analysis, writing – review & editing, project administration, funding acquisition, supervision.

Conflicts of interest

The authors declare no competing interest.

Acknowledgements

References

1 A. Sciortino, A. Cannizzo and F. Messina, *C*, 2018, **4**, 67.
2 A. Cayuela, M. L. Soriano, C. Carrillo-Carrion and M. Valcarcel, *Chem. Commun.*, 2016, **52**, 1311–1326.
3 Y. Park, J. Yoo, B. Lim, W. Kwon and S. W. Rhee, *J. Mater. Chem. A*, 2016, **4**, 11582–11603.
4 J. Zhang and S. H. Yu, *Mater. Today*, 2016, **19**, 382–393.
5 W. Lu, X. Gong, Z. Yang, Y. Zhang, Q. Hu, S. Shuang, C. Dong and M. M. F. Choi, *RSC Adv.*, 2015, **5**, 16972–16979.
6 A. V. Longo, A. Sciortino, M. Cannas and F. Messina, *Phys. Chem. Chem. Phys.*, 2020, **22**, 13398–13407.
7 A. Sharma and J. Das, *J. Nanobiotechnol.*, 2019, **17**, 92.
8 L. Sai, J. Chen, Q. Chang, W. Shi, Q. Chen and L. Huang, *RSC Adv.*, 2017, **7**, 16608–16615.
9 W. Wang, C. Damm, J. Walter, T. J. Nacken and W. Peukert, *Phys. Chem. Chem. Phys.*, 2016, **18**, 466–475.
10 Q. Ren, L. Ga and J. Ai, *ACS Omega*, 2019, **4**, 15842–15848.
11 M. Varisco, D. Zufferey, A. Ruggi, Y. Zhang, R. Erni and O. Mamula, *R. Soc. Open Sci.*, 2017, **4**, 170900.
12 K. M. Omer, S. A. Idrees, A. Q. Hassan and L. A. Jamil, *New J. Chem.*, 2020, **44**, 5120–5126.
13 M. Li, Y. Feng, Q. Tian, W. Yao, L. Liu, X. Li, H. Wang and W. Wu, *Dalton Trans.*, 2018, **47**, 11264–11271.
14 Z. J. Wang, X. J. Zhao, Z. Z. Guo, P. Miao and X. Gong, *Org. Electron.*, 2018, **62**, 284–289.
15 A. G. El-Shamy and H. S. S. Zayied, *Synth. Met.*, 2020, **259**, 116218.
16 M. A. Issa and Z. Z. Abidin, *Molecules*, 2020, **25**, 3541.
17 S. Lu, L. Sui, J. Liu, S. Zhu, A. Chen, M. Jin and B. Yang, *Adv. Mater.*, 2017, **29**, 1603443.
18 P. Gupta, M. Bera and P. K. Maji, *Polym. Adv. Technol.*, 2017, **28**, 1428–1437.
19 J. Andres, R. D. Hersch, J.-E. Moser and A. S. Chauvin, *Adv. Funct. Mater.*, 2014, **24**, 5029–5036.
20 K. T. P. Lim, H. Liu, Y. Liu and J. K. W. Yang, *Nat. Commun.*, 2019, **10**, 25.
21 J. Y. Park, J. W. Chung and H. K. Yang, *Ceram. Int.*, 2019, **45**, 11591–11599.
22 F. Liu, Z. Li, Y. Li, Y. Feng and W. Feng, *Carbon*, 2021, **181**, 9–15.

23 P. Kumar, S. Singh and B. K. Gupta, *Nanoscale*, 2016, **8**, 14297–14340.

24 Z. Zhang, W. Sun and P. Wu, *ACS Sustainable Chem. Eng.*, 2015, **3**, 1412–1418.

25 J. Guo, H. Li, L. Ling, G. Li, R. Cheng, X. Lu, A.-Q. Xie, Q. Li, C.-F. Wang and S. Chen, *ACS Sustainable Chem. Eng.*, 2020, **8**, 1566–1572.

26 J.-x. Zheng, X.-h. Liu, Y.-z. Yang, X.-g. Liu and B.-s. Xu, *New Carbon Mater.*, 2018, **33**, 276–288.

27 Y. Ma, X. Zhang, J. Bai, K. Huang and L. Ren, *Chem. Eng. J.*, 2019, **374**, 787–792.

28 S. S. Jones, P. Sahatiya and S. Badhulika, *New J. Chem.*, 2017, **41**, 13130–13139.

29 W. T. Hong and H. K. Yang, *Optik*, 2021, **241**, 166449.

30 M. He, J. Zhang, H. Wang, Y. Kong, Y. Xiao and W. Xu, *Nanoscale Res. Lett.*, 2018, **13**, 175.

31 H. Li, Y. Xu, L. Zhao, J. Ding, M. Chen, G. Chen, Y. Li and L. Dang, *Carbon*, 2019, **143**, 391–401.

32 N. K. Sahoo, G. C. Jana, M. N. Aktara, S. Das, S. Nayim, A. Patra, P. Bhatttacharjee, K. Bhadra and M. Hossain, *Mater. Sci. Eng., C*, 2020, **108**, 110429.

33 L. Cadesky, M. W. Ribeiro, K. T. Kriner, M. V. Karwe and C. I. Moraru, *J. Dairy Sci.*, 2017, **100**, 7055–7070.

34 M. Warncke and U. Kulozik, *Foods*, 2021, **10**, 1361.

35 Y. T. Xie, J. X. Zheng, Y. L. Wang, J. L. Wan, Y. Z. Yang, X. G. Liu and Y. K. Chen, *Nanotechnology*, 2019, **30**, 085406.

36 A. Pal, M. P. Sk and A. Chattopadhyay, *Mater. Adv.*, 2020, **1**, 525–553.

37 B. Zhang, Y. Liu, M. Ren, W. Li, X. Zhang, R. Vajtai, P. M. Ajayan, J. M. Tour and L. Wang, *ChemSusChem*, 2019, **12**, 4202–4210.

38 K. J. Mintz, M. Bartoli, M. Rovere, Y. Zhou, S. D. Hettiarachchi, S. Paudyal, J. Chen, J. B. Domena, P. Y. Liyanage, R. Sampson, D. Khadka, R. R. Pandey, S. Huang, C. C. Chusuei, A. Tagliaferro and R. M. Leblanc, *Carbon*, 2021, **173**, 433–447.

39 R. Bandi, B. R. Gangapuram, R. Dadigala, R. Eslavath, S. S. Singh and V. Guttena, *RSC Adv.*, 2016, **6**, 28633–28639.

40 F. Victoria, J. Manioudakis, L. Zaroubi, B. Findlay and R. Naccache, *RSC Adv.*, 2020, **10**, 32202–32210.

41 J. Ederer, P. Janoš, P. Ecorchard, J. Tolasz, V. Štengl, H. Beneš, M. Perchacz and O. Pop-Georgievski, *RSC Adv.*, 2017, **7**, 12464–12473.

42 D. M. Eby, K. Artyushkova, A. K. Paravastu and G. R. Johnson, *J. Mater. Chem.*, 2012, **22**, 9875–9883.

43 C. Wang, C. Wang, P. Xu, A. Li, Y. Chen and K. Zhuo, *J. Mater. Sci.*, 2016, **51**, 861–867.

44 D. Xu, F. Lei, H. Chen, L. Yin, Y. Shi and J. Xie, *RSC Adv.*, 2019, **9**, 8290–8299.

45 A. P. Sirocic, L. K. Krehula, Z. Katancic and Z. H. Murgj, *Chem. Biochem. Eng. Q.*, 2017, **30**, 501–509.

46 P. K. Sarswat and M. L. Free, *Phys. Chem. Chem. Phys.*, 2015, **17**, 27642–27652.

47 D. L. Vien, N. Colthup, W. Fateley and J. Grasselli, *The Handbook of Infrared and Raman Characteristic Frequencies of Organic Molecules*, Academic Press, Boston, 1991.

48 C. Zhu, J. Zhai and S. Dong, *Chem. Commun.*, 2012, **48**, 9367–9369.

49 B. Manoj, A. M. Raj and G. T. Chirayil, *Sci. Rep.*, 2017, **7**, 18012.

50 I. J. Gomez, M. V. Sullerio, A. Doleckova, N. Pizurova, J. Medalova, R. Roy, D. Necas and L. Zajickova, *J. Phys. Chem. C*, 2021, **125**, 21044–21054.

51 C. M. Carbonaro, R. Corpino, M. Salis, F. Mocci, S. V. Thakkar, C. Olla and P. C. Ricci, *C*, 2019, **5**, 60.

52 J. T. Margraf, V. Strauss, D. M. Guldi and T. Clark, *J. Phys. Chem. B*, 2015, **119**, 7258–7265.

53 G. D. Gesesse, A. G. Berenguer, M.-F. Barthe and C. O. Ania, *J. Photochem. Photobiol., A*, 2020, **398**, 112622.

54 K. J. Mintz, Y. Zhou and R. M. Leblanc, *Nanoscale*, 2019, **11**, 4634–4652.

55 J. Tauc, R. Grigorovici and A. Vancu, *Phys. Status Solidi*, 1966, **15**, 627–637.

56 C. Murru, R. Badia-Laino and M. E. D. Garcia, *Antioxidants*, 2020, **9**, 1147.

57 D. D. Ferreyra, D. R. Sartori, S. D. E. Riega, H. B. Rodriguez and M. C. Gonzalez, *Carbon*, 2020, **167**, 230–243.

58 D. L. Wood and J. Tauc, Weak Absorption Tails in Amorphous Semiconductors, *Phys. Rev. B: Solid State*, 1972, **5**, 3144–3151.

59 I. Studenyak, M. Kranjec and M. Kurik, *Int. J. Opt. Appl.*, 2014, **4**, 76–83.

60 K. P. Neha Sharma, S. Ilango, S. Dash and A. K. Tyagi, *Advanced Materials Proceedings*, 2017, **2**, 342–346.

61 Y. P. Sun, B. Zhou, Y. Lin, W. Wang, K. A. S. Fernando, P. Pathak, M. J. Meziani, B. A. Harruff, X. Wang, H. F. Wang, P. J. G. Luo, H. Yang, M. E. Kose, B. L. Chen, L. M. Veca and S. Y. Xie, *J. Am. Chem. Soc.*, 2006, **128**, 7756–7757.

62 B. Manoj, A. M. Raj and G. C. Thomas, *Sci. Rep.*, 2018, **8**, 13891.

63 S. Zhu, Y. Song, X. Zhao, J. Shao, J. Zhang and B. Yang, *Nano Res.*, 2015, **8**, 355–381.

64 B. Zhi, X. X. Yao, Y. Cui, G. Orr and C. L. Haynes, *Nanoscale*, 2019, **11**, 20411–20428.

65 Y. H. Liu, H. Huang, W. J. Cao, B. D. Mao, Y. Liu and Z. H. Kang, *Mater. Chem. Front.*, 2020, **4**, 1586–1613.

66 J. R. Lakowicz, *Principles of fluorescence spectroscopy*, Springer, USA, 2006.

67 J. R. Alcala, E. Gratton and F. G. Prendergast, *Biophys. J.*, 1987, **51**, 597–604.

68 S. Kalytchuk, Y. Wang, K. Polakova and R. Zboril, *ACS Appl. Mater. Interfaces*, 2018, **10**, 29902–29908.

69 T. Yu, H. Wang, C. Guo, Y. Zhai, J. Yang and J. Yuan, *R. Soc. Open Sci.*, 2018, **5**, 180245.

70 X. Liu, T. Z. Li, Y. Hou, Q. H. Wu, J. Yi and G. L. Zhang, *RSC Adv.*, 2016, **6**, 11711–11718.

71 P. F. Fox and A. Brodkorb, *Int. Dairy J.*, 2008, **18**, 677–684.

72 C. Phadungath, *Songklanakarin J. Sci. Technol.*, 2004, **27**, 201–212.

73 J. R. Dios, C. G. Astrain, P. Costa, J. C. Viana and S. L. Mendez, *Materials*, 2019, **12**, 1405.

74 L. Jun, L. Qiaochu, Q. Rongrong and S. Yanhan, *China Pat.*, CN100564416C, 2009.